Modelling and Simulation in Materials Science and Engineering

Microchemistry-dependent simulation of yield stress and flow stress in non-heat treatable Al sheet alloys

OPEN ACCESS
IOP Publishing
Modelling and Simulation in Materials Science and Engineering
Modelling Simul. Mater. Sci. Eng. **28** (2020) 035010 (21pp) https://doi.org/10.1088/1361-651X/ab71c0

Microchemistry-dependent simulation of yield stress and flow stress in non-heat treatable Al sheet alloys

Su Leen Wong[1], Galyna Laptyeva[2], Thiemo Brüggemann[2], Olaf Engler[2], Franz Roters[1], Dierk Raabe[1] and Kai-Friedrich Karhausen[2]

[1] Max-Plank-Institut für Eisenforschung, Department of Microstructure Physics and Alloy Design, D-40237, Düsseldorf, Germany
[2] Hydro Aluminium Rolled Products GmbH, Research and Development Bonn, D-53014, Bonn, Germany

E-mail: s.wong@mpie.de

Received 13 November 2019, revised 24 January 2020
Accepted for publication 30 January 2020
Published 18 February 2020

Abstract

A flow stress model which considers the processing conditions for a given alloy composition as well as the microchemistry of the alloy allows for integrated optimization of alloy composition, thermal treatments and forming operations to achieve the desired properties in the most efficient processing route. In the past, a statistical flow stress model for cell forming metals, 3IVM+ (3 Internal Variable Model), has been used for through process modeling of sheet production. However, this model was restricted to a given alloy in the state in which it was calibrated. In this work, the existing 3IVM+ model is augmented with an analytical solute strengthening model which uses input from *ab initio* simulations. Furthermore, a new particle strengthening model for non-shearable precipitates has been introduced which takes Orowan looping at low temperatures and dislocation climb at high temperatures into account. Hence, the present modeling approach considers the strengthening contributions from solutes, precipitates and forest dislocations. Three case studies on the alloys AA 1110, AA 3003 and AA 8014 are presented to assess the performance of the model in simulating the yield stress and flow stress of Al alloys over a wide range of temperatures and strain rates.

Keywords: yield strength, flow stress, solutes, particles, wrought alloys, dislocations, simulation

(Some figures may appear in colour only in the online journal)

1. Introduction

Aluminum with its various alloy variations is a first-choice material for a number of lightweight engineering applications. Besides high relative strength and excellent ductility, it offers further advantageous properties such as corrosion resistance, high electrical and thermal conductivity, high reflectivity, impermeability and good recyclability.

Innovation goes hand in hand with growing expectations and requirements from customers on the quality of aluminum semi-finished products, such as sheet, strips or extrusions. In the aluminum industry, reliable and efficient manufacturing processes are the main prerequisites to fulfill growing expectations on semi-finished products in a strong field of worldwide competition.

From this standpoint, the employment of *computer-aided decision-making systems* in the process routing or even at a shop floor level are desired. Systems of this kind enable an automatic adjustment of the process parameters making the industrial manufacturing processes more flexible, assuring achievement of the desired properties. Gapless process and material data acquisition is necessary for a functioning decision-making system. State-of-the-art semi-finished aluminum production typically utilizes advanced sensor technology, enabling the acquisition of comprehensive production data. However, the material properties of aluminum semi-finished products cannot be easily measured during the production process. To close this data gap, fast statistical material models can be used to compute material properties such as the microstructure and flow stress.

To predict the flow stress by means of a statistical material model, a three internal variable model (3IVM) has been developed by Roters *et al* [1] and thereafter further refined (3IVM+) [2–5]. In the present work, the 3IVM+ model and its current improvements are discussed. New expressions have been introduced for the contribution of solute strengthening and particle strengthening to the flow stress in order to render the model microchemistry-dependent. Finally, three case studies are presented on industrial aluminum alloys, i.e. AA 1110, AA 3103 and AA 8014, to assess the quality of the simulations of the yield stress and flow stress at different temperatures ranging from 20 °C to 550 °C and for three different strain rates ranging from 0.1 to 10 s^{-1}.

2. Modeling of flow stress

Considering the main strengthening mechanisms of Al alloys and further assuming that the contribution of these mechanisms can simply be added linearly in stress space [6–8], the macroscopic flow stress, σ, can be written as:

$$\sigma = \sigma_{\text{int}} + \sigma_{\text{sol}} + \sigma_{\text{par}} + \sigma_{\text{for}}, \tag{1}$$

where σ_{int} is the intrinsic stress of Al, σ_{sol} is the flow stress contribution due to solute strengthening, σ_{par} is the flow stress contribution due to particle strengthening and σ_{for} is the flow stress contribution due to forest dislocations.

The 3IVM model was originally developed by Roters *et al* [1], which was further improved by Mohles *et al* [4] resulting in the 3IVM+ model. The model presented in this

work builds upon the 3IVM+ model, incorporates a solute strengthening model developed by Leyson *et al* [9–12] and introduces a new particle strengthening model which captures Orowan looping at low temperatures and dislocation climb at high temperatures.

In the following sections, the solid solution strengthening model by Leyson *et al* [9–12] is first summarized in section 2.1. The new particle strengthening model and the temperature dependence of the intrinsic stress are introduced in section 2.2. Finally, the work hardening model based on the 3IVM+ and the kinetic equation of state are described in section 2.3.

2.1. Solid solution strengthening

Solid solution strengthening is commonly attributed to the interaction of dislocations with their surrounding solute alloy elements due to their misfit volume and elastic mismatch. This gives rise to the pinning of dislocations, which consequently leads to higher external stresses required to move the dislocations through the crystal lattice. There are various approaches to model the strengthening as a function of the concentration of alloying elements in solid solution. The most commonly utilized approaches date back to Fleischer [13] and Labusch [14], where the solid solution strength, σ_{sol}, scales with the concentration of solute elements, c:

$$\sigma_{\text{sol}} = Kc^n, \tag{2}$$

where K is a constant and n is an exponent in the range of $1/2$ to $2/3$.

Previous versions of 3IVM+ utilized the approach of equation (2) [3–5], however the influence of several different alloying elements in solid solution, as typically found in commercial Al alloys, cannot be treated independently. This approach also involves a number of parameters which have to be calibrated for each alloy.

An analytical solute strengthening model which predicts the strengthening of Al due to substitutional solute atoms has been developed by Leyson *et al* [9–12]. This model uses input from first principles computations, enabling a quantitative prediction of the yield stress in binary and multicomponent alloy systems with considerable solute strengthening. This model has been validated for the following systems: Al–Mg, Al–Cu, Al–Cr, Al–Si, and Al–Mg–Si with Fe [9–11]. In this section, the solid solution strengthening model used in the current work is briefly summarized.

Dislocation segments in a random field of solutes are typically pinned to energetically favorable solute field regions, which correspond to a favorable interaction energy between dislocation and solute. When an external stress is applied and a dislocation starts moving on its slip plane through a field of solutes, an additional stress is required to 'unpin' the dislocation from these favorable solute regions. Density functional theory calculations were used by Leyson *et al* [9, 10] to compute the zero-temperature yield stress, σ_{y0}, and the energy barrier, ΔE_b, required for dislocation motion. Table 1 shows these two quantities calculated as a function of the solute concentration, c, for the main alloying elements in Al, including Mg, Cr, Si, Cu, Mn, and Fe.

It is noted that Leyson *et al* [10] found that the strengths of Al–Fe alloys containing merely parts per million (ppm) of Fe solutes were grossly underestimated. They concluded that strengthening due to dilute Fe solutes cannot be treated by conventional *ab initio* models, possibly due to directional bonding between the Fe and Al atoms within the dislocation core. However, the experimental yield stresses for Al–Fe still scaled reasonably well with $c^{2/3}$, suggesting that the same scaling applies to the Fe solutes despite the anomalous magnitude. Therefore, Leyson *et al* [10] recalculated the parameters for solute Fe from experimental data [15]. However, in the present study it was found that the recalculated values for Fe yield too

Table 1. *Ab initio* calculated zero-temperature yield stress, σ_{y0}, and energy barrier, ΔE_B, normalized by the solute concentration, c, in atomic fraction for different solutes in Al. Data reproduced from Leyson *et al* [10]. Parameters in bold for Fe solutes were calibrated to fit the experimental data; see text for details.

Solute	$\boldsymbol{\sigma_{y0}/c^{2/3}}$ (MPa)	$\boldsymbol{\Delta E_b/c^{1/3}}$ (eV)
Mg	342	4.06
Cr	705	6.65
Si	137	2.58
Cu	348	4.10
Mn	711	7.53
Fe	1072 (**11 252**)	8.20 (**24.5**)

large values for the solute strength. Therefore, we applied a scaling factor of 0.85 to Leyson's recalculated values, which resulted in more reasonable predictions for the yield stress of all three alloys. The resulting values used for Fe throughout the present study are also given in table 1 (in bold).

In multicomponent alloys with n different solute types in solid solution, the zero-temperature yield stress and energy barrier are calculated respectively as follows [9, 10]:

$$\sigma_{y0} = \left[\sum_{i=1}^{n} (\sigma^i_{y0})^{\frac{3}{2}}\right]^{\frac{2}{3}}, \tag{3}$$

$$\Delta E_b = \left[\sum_{i=1}^{n} (\Delta E^i_b)^3\right]^{\frac{1}{3}}, \tag{4}$$

where the superscript i denotes the quantity for solute i.

The stress-dependent energy barrier has the form [16, 17]:

$$\Delta E(\sigma) = \Delta E_b \left[1 - \left(\frac{\sigma}{\sigma_{y0}}\right)\right]^{\frac{3}{2}}. \tag{5}$$

Equation (5) is valid only for high stresses and low temperatures with $\frac{\sigma_y}{\sigma_{y0}} > 0.5$. The experiments conducted in the present study were performed at intermediate temperatures, corresponding to lower flow stresses in the range $0.2 < \frac{\sigma_y}{\sigma_{y0}} < 0.5$. In this case, the energy barrier as a function of stress can better be approximated by a logarithmic relationship [12]:

$$\Delta E(\sigma) = 0.55\ \Delta E_b \ln\left(\frac{\sigma}{\sigma_{y0}}\right). \tag{6}$$

Using the Arrhenius model for thermal activation, the energy barrier is related to the strain rate $\dot{\varepsilon}$ through:

$$\dot{\epsilon} = \dot{\epsilon}_0 \exp\left(\frac{-\Delta E(\sigma)}{k_B T}\right), \tag{7}$$

where $\dot{\varepsilon}_0$ is a reference strain rate, k_B is the Boltzmann constant and T is the temperature.

The Orowan equation is used as the kinetic equation of state:

$$\dot{\gamma} = \dot{\epsilon}M = \rho_m b v(T), \tag{8}$$

where $\dot{\gamma}$ is the shear rate.

The average dislocation glide velocity, $v(T)$, is expressed as:

$$v(T) = L_{\text{eff}}\upsilon_0 \exp\left(\frac{-\Delta E}{k_B T}\right), \tag{9}$$

where υ_0 is the attack frequency (3×10^{10} Hz) and L_{eff} is the mean free path for dislocation motion.

Using equations (7)–(9), the reference strain rate $\dot{\varepsilon}_0$ can be expressed as:

$$\dot{\epsilon}_0 = \frac{\rho_m b L_{\text{eff}} \nu_0}{M}, \tag{10}$$

where b is the magnitude of the Burgers vector, M is the Taylor factor, L_{eff} is the mean free path of dislocation motion and υ_0 is the attack frequency (3×10^{10} Hz).

Substituting equations (7) and (10) into (6) and inverting the latter provides an expression for the stress, σ_{sol}, required to move a dislocation through a random field of solutes at a finite temperature, T [12]:

$$\sigma_{\text{sol}} = \sigma_{y0} \exp\left(-\frac{1}{0.55}\frac{k_B T}{\Delta E_b} \ln \frac{\dot{\varepsilon}_0}{\dot{\varepsilon}}\right). \tag{11}$$

This equation—simply referred to as Leyson model hereafter—is used for the simulation of the contribution of solid solution strengthening in the present study.

2.2. Particle strengthening and intrinsic strength

Most commercial aluminum alloys contain particles, such as constituent phases formed during solidification, dispersoids formed during homogenization and fine precipitates formed during age hardening at low temperatures. The contribution of these second-phase particles to the flow stress is assumed to be additive as in equation (1).

The strength contribution due to non-shearable particles, i.e. constituents and dispersoids, is derived from the Orowan mechanism of dislocations bypassing particles. According to Deschamps and Brechet [18], the increase in yield strength, τ_{Or}, is related to the obstacle strength, F, as follows:

$$\tau_{\text{Or}} = \frac{F}{bl}, \tag{12}$$

where l is the mean effective particle spacing in the slip plane along the bending dislocation. For strong non-shearable particles, the obstacle strength F is related to the line tension of a dislocation, i.e.:

$$F = 2\beta\mu b^2, \tag{13}$$

where μ is the temperature-dependent shear modulus of aluminum and β is a geometric constant close to 0.5. Using the Friedel formalism [19], the effective particle spacing l can be related to the mean particle size r_{p} and the volume fraction V_{P} of the particles. Thus, equation (12) becomes:

$$\sigma_{\mathrm{OR}} = \sqrt{\frac{6}{\pi}} M\beta\mu b \frac{\sqrt{V_{\mathrm{p}}}}{r_{\mathrm{p}}}. \tag{14}$$

It is noted that the Orowan stress in equation (14) is applicable at room temperature (RT). As the test temperature increases the particle strengthening mechanism transitions from Orowan looping at low temperatures to dislocation climb over particles at high temperatures [20]. Thus, the particle strengthening contribution to the flow stress σ_{par}, and its temperature dependence, is modeled using the following phenomenological equation:

$$\sigma_{\mathrm{par}}(T) = \sigma_{\mathrm{OR}}\left[1 - \exp\left(\frac{-T_{\mathrm{crit}}}{T}\right)^{A}\right], \tag{15}$$

where T is the current temperature, T_{crit} is the transition temperature between Orowan looping and dislocation climb and A is a parameter which controls the steepness of the transition from Orowan looping to dislocation climb.

The intrinsic stress is assumed to have the same form of the temperature dependence as the particle stress, since it is difficult to separate the temperature dependence of these two contributions to the flow stress. Experiments in pure copper [21, 22] have shown a similar temperature dependence of the yield stress which, in the absence of particles or precipitates in the material, can be attributed to the intrinsic stress. Therefore, the temperature dependence of the intrinsic stress is similarly expressed as:

$$\sigma_{\mathrm{int}}(T) = \sigma_0\left[1 - \exp\left(\frac{-T_{\mathrm{crit}}}{T}\right)^{A}\right], \tag{16}$$

where σ_0 is the intrinsic or lattice friction stress at RT for Al, typically estimated as 10 MPa [23–25]. Due to the difficulty in isolating the temperature dependence of the intrinsic stress solely from the experimental yield stress data, the same values for T_{crit} and A as those used in the Orowan stress equation (equation (15)) are also used in equation (16).

2.3. Work hardening

During deformation, the strength of metals and alloys increases due to work hardening, which is caused by the increase in dislocation density within the material. The evolution of the dislocation density during deformation is simulated using the 3IVM+ model (3 Internal Variable Model) [2–5], which was developed to predict the flow stress evolution in cell forming metals, such as Al and Al alloys. In this section, the model in its current implementation is summarized.

The microstructure of the material in 3IVM+ is represented by three internal state variables: the mobile dislocation density (ρ_m), the immobile dislocation density in the cell interior (ρ_i) and the immobile dislocation density in the cell wall (ρ_w). The governing equations for a statistical internal state variable model consist of the evolution equations for the dislocation densities and the kinetic equation of state, where the latter determines the external stress required to accommodate an imposed strain rate on the material for a given temperature and microstructure during an infinitely small time increment. While the evolution equations of the dislocation densities in this model are largely unchanged from the original 3IVM+ model, the calculation of the stress in the cell wall and cell interior is currently based on the model by Dong *et al* [26], which enables the incorporation of the solute strengthening model by Leyson *et al* [9–12] (see section 2.1).

The rate of evolution of the dislocation densities is represented as:

$$\dot{\rho}_x = \dot{\rho}_x^+ - \dot{\rho}_x^-, \tag{17}$$

where the indices $x = m,\ i,\ w$ correspond to mobile, cell interior and cell wall respectively; $\dot{\rho}_x^+$ is the production rate for a particular dislocation density type and $\dot{\rho}_x^-$ is the reduction or recovery rate for a particular dislocation density type.

During deformation, dislocations move through the lattice and a number of interactions take place (i.e. annihilation, dipole formation, lock formation, immobilization, climb, cross slip and clearing). The evolution of the dislocation densities is summarized as follows, where additional details can be found in [5].

$$\begin{aligned}\dot{\rho}_m = {} & \dot{\rho}_m^+ - \dot{\rho}_m^-(\text{anni}) - \dot{\rho}_m^-(\text{dipole}) \\ & - \dot{\rho}_m^-(\text{lock}) - \dot{\rho}_m^-(\text{imm})\end{aligned} \tag{18a}$$

$$\begin{aligned}\dot{\rho}_i = {} & \dot{\rho}_i^+(\text{lock}) + \dot{\rho}_i^+(\text{imm}) - \dot{\rho}_i^-(\text{climb}) \\ & - \dot{\rho}_i^-(\text{cross}) - \dot{\rho}_i^-(\text{clear})\end{aligned} \tag{18b}$$

$$\begin{aligned}\dot{\rho}_w = {} & \dot{\rho}_w^+(\text{lock}) + \dot{\rho}_w^+(\text{dipole}) + \dot{\rho}_w^+(\text{imm}) \\ & - \dot{\rho}_w^-(\text{climb}) - \dot{\rho}_w^-(\text{cross}) - \dot{\rho}_w^-(\text{clear}).\end{aligned} \tag{18c)}$$

Mobile dislocations carry plastic strain. They are assumed to penetrate both the cell walls and the cell interiors. Each mobile dislocation is assumed to travel a certain distance, L_{eff}, before it is immobilized or annihilated. Following the approach of Roters *et al* [1], the mean free path L_{eff} is determined by the effective grain size d and three obstacle spacings, i.e. the forest dislocation spacing in the cell walls, the forest dislocation spacing in the cell interior and the average particle spacing. Thus, the effective mean free path of mobile dislocations, L_{eff}, is calculated as follows:

$$\begin{aligned}\frac{1}{L_{\text{eff}}} = {} & \frac{1}{d} + \sqrt{\rho_i + \rho_m}\frac{(1 - f_w)}{\beta_i} \\ & + \sqrt{\rho_w + \rho_m}\frac{f_w}{\beta_w} + \frac{1}{r_{\text{p}}}\sqrt{\frac{3V_{\text{p}}}{2\pi}},\end{aligned} \tag{19}$$

where β_i and β_w are model parameters which quantify the average number of dislocation spacings which a dislocation travels before becoming sessile; and V_{p} and r_{p} are the volume fraction and mean radius of the non-shearable particles. The volume fractions of the cell interiors and cell walls are given as f_i and $f_w = 1 - f_i$, respectively.

The calculation of the stress in the cell walls and cell interiors is based on the approach by Dong *et al* [26]. At the flow stress, the rates of dislocations escaping from solutes and forest dislocations are assumed to be equal, therefore the respective activation energies ΔG_{sol} and ΔG_{for} are equal as well:

$$\Delta G = \Delta G_{\text{sol}} = \Delta G_{\text{for}}. \tag{20}$$

The activation energies to escape from randomly distributed weak obstacles (solutes) and from a linear array of obstacles (forest dislocations) are given as follows:

$$\Delta G_{\text{sol}} = \Delta G_{\text{sol}}^0\left(1 - \left(\frac{\tau_{\text{sol}}}{\hat{\tau}_{\text{sol}}}\right)^{\frac{2}{3}}\right)^{\frac{3}{2}}, \tag{21a}$$

$$\Delta G_{\text{for}} = \Delta G^0_{\text{for}} \left(1 - \frac{\tau_{\text{for}}}{\hat{\tau}_{\text{for}}}\right)^{\frac{3}{2}}, \tag{21b}$$

where $\hat{\tau}_{\text{sol}}$ is the threshold stress due to solutes and $\hat{\tau}_{\text{for}}$ represents the threshold stress contribution due to the current dislocation substructure ($\hat{\tau}_{\text{for}} \propto \mu b\sqrt{\rho}$).

For thermally activated flow, again assuming linear additivity, it holds:

$$\tau_{\text{ther}} = \tau_{\text{sol}} + \tau_{\text{for}}. \tag{22}$$

Substituting equation (22) in (21*a*) and using equation (20) yields:

$$\begin{aligned} \Delta G &= \Delta G^0_{\text{sol}} \left(1 - \left(\frac{\tau_{\text{ther}} - \tau_{\text{for}}}{\hat{\tau}_{\text{sol}}}\right)^{\frac{2}{3}}\right)^{\frac{3}{2}} \\ &= \Delta G^0_{\text{for}} \left(1 - \frac{\tau_{\text{for}}}{\hat{\tau}_{\text{for}}}\right)^{\frac{3}{2}}. \end{aligned} \tag{23}$$

Equation (23) can then be solved for τ_{ther}:

$$\tau_{\text{ther}} = \left(1 - \left(\frac{\Delta G}{\Delta G^0_{\text{sol}}}\right)^{\frac{2}{3}}\right)^{\frac{3}{2}} \hat{\tau}_{\text{sol}} + \left(1 - \left(\frac{\Delta G}{\Delta G^0_{\text{for}}}\right)^{\frac{2}{3}}\right) \hat{\tau}_{\text{for}}. \tag{24}$$

The first term on the right side of equation (24) is the solute contribution to the stress, τ_{sol}, and the second term is the stress due to the forest dislocation density, τ_{for}. Substituting equation (7) in (24) and (24) in (22), gives:

$$\tau_{\text{ther}} = \tau_{\text{sol}} + \left[1 - \left(\frac{k_B T}{\Delta G^0_{\text{for}}} \ln \frac{\dot{\varepsilon}_0}{\dot{\varepsilon}}\right)^{\frac{2}{3}}\right] \hat{\tau}_{\text{for}}. \tag{25}$$

The stress due to forest dislocations in the cell interior and cell wall is written as:

$$\tau^{i,w}_{\text{for}} = \left[1 - \left(\frac{k_B T}{\Delta G^0_{\text{for}}} \ln \frac{\dot{\epsilon}_0}{\dot{\epsilon}}\right)^{2/3}\right] \hat{\tau}_{\text{for}}, \tag{26}$$

where ΔG^0_{for} is a fitting parameter and *i, w* denote the cell interior and cell wall, respectively.

The threshold stress due to the dislocation substructure, $\hat{\tau}_{\text{for}}$, is assumed to be equal to the Taylor stress in the cell interior and cell wall:

$$\hat{\tau}_{\text{for}} = \tau^{i,w}_{\text{Taylor}} = \alpha \mu b \sqrt{\rho_m + \rho_{i,w}}, \tag{27}$$

where α is the passing coefficient for shear.

The stress in the cell wall and cell interior can be expressed as:

$$\tau_{i,w} = \left[1 - \left(\frac{k_{\text{B}} T}{Q_{\text{slip}}} \ln \frac{\dot{\epsilon}_0}{\dot{\epsilon}}\right)^{2/3}\right] \tau^{i,w}_{\text{taylor}} + \tau_{\text{sol}} + \tau_{\text{par}} + \tau_{\text{int}}. \tag{28}$$

The total macroscopic flow stress, σ_{tot} is calculated using the following equation:

$$\sigma_{\text{tot}} = M(f_i \tau_i + f_w \tau_w). \tag{29}$$

Table 2. Chemical composition of the AA 1110, AA 3103 and AA 8014 alloys (in wt%, remainder: Al).

Element	Si	Fe	Cu	Mn	Mg	Cr	Zn	Ti
AA 1110	0.087	0.38	0.0017	0.003	0.216	0.001	0.013	0.007
AA 3103	0.063	0.53	0.0027	1.030	0.010	0.0006	0.0054	0.006
AA 8014	0.056	1.23	0.0006	0.34	0.002	0.0006	0.012	0.003

Using equations (28), (29) can also be written as:

$$\sigma_{\text{tot}} = M\left(f_i \tau_{\text{for}}^{i} + f_w \tau_{\text{for}}^{w}\right) + \sigma_{\text{sol}} + \sigma_{\text{par}} + \sigma_{\text{int}} \tag{30}$$

with σ_{sol} from equation (11), σ_{par} from equation (15) and σ_{int} from equation (16). The resulting equation (30) is equivalent to the simple additive stress equation shown in equation (1).

3. Materials and experimental techniques

Three different Al alloys with different solute and particle content were analyzed as case studies. The chemical compositions of the three alloys, i.e. AA 1110, AA 3103 and AA 8014, are given in table 2. Alloy AA 1110 is an Al–Fe–Si alloy which comprises large particles which do not contribute significantly to the overall strength. Furthermore, AA 1110 contains around 0.2% of Mg which provides some solute strengthening. Most notably, however, the strength of AA 1xxx series alloys is derived from strain hardening to various tempers H1x. Alloy AA 3103 is an Al–Mn alloy which contains some Mn in solid solution and contains a fairly large volume of Mn-bearing dispersoids which provide additional particle strengthening. Finally, alloy AA 8014 contains significant amounts of Fe and Mn, leading to a combination of solid solution hardening and dispersoid hardening.

In the present study, transfer gauge material of the three alloys taken from an industrial hot mill was investigated. The alloys were conventionally direct-chill (DC) cast, homogenized and then hot rolled on a reversible hot mill to a thickness of approximately 35 mm. The experimental flow curves were obtained by means of isothermal uniaxial compression tests of cylindrical specimens (30 mm height and 20 mm diameter) on a Servotest hydraulic press at the Institute for Metal Forming, RWTH Aachen University. The specimens for the compression tests were machined from the transfer slab material and rehomogenized at 550 °C for 20 min. To conduct the compression tests the samples were then cooled to the desired temperature in the range of RT to 550 °C and compressed at a constant controlled strain rate of 0.1, 1.0 or 10 s^{-1}. To reduce friction between the sample and the punch, a Teflon foil was used in the temperature range between RT and 350 °C. At higher temperatures of 400 to 550 °C, boron nitride lubrication was used.

The solute concentration of the alloys was determined by a combination of specific electrical resistivity and thermoelectric power measurements. The specific electrical resistivity, ρ, was measured in liquid helium at a temperature of 4.2 K. The thermoelectric power, TEP, is the thermoelectric voltage in response to a temperature difference, typically $\Delta T = 10$ K, across the material (Seebeck effect). Since the specific TEP signals of individual alloy elements vary with temperature in different ways, TEP values obtained at various subambient temperatures can provide a sufficient number of independent measurements for the solute levels in multi-component Al alloys [27, 28]. Table 3 lists the resulting concentration of solute elements for the three alloys of the present study.

Table 3. Concentration of solute elements for the three alloys in the present study as obtained from TEP measurements (in wt%).

	Si	Fe	Cu	Mn	Mg	Cr	Zn	Ti
AA 1110	0.035	0.004	0.0012	0.0026	0.174	0.0005	0.0103	0.0061
AA 3103	0.020	0.010	0.0023	0.35	0.0076	0.0006	0.0039	0.0047
AA 8014	0.0016	0.0074	0.0001	0.0765	0.0002	0.0001	0.0007	0.0003

Table 4. Particle volume fraction and radius for the three alloys analyzed in the present study.

Alloy	Particle volume fraction, V_p	Particle radius, r_p (μm)
AA 1110	0.010	0.400
AA 3103	0.003	0.075
AA 8014	0.0042	0.115

The constituent particles in alloy AA 1110 were analyzed using standard metallographic techniques in an optical microscope and evaluated quantitatively with the image analysis software package Quantimet 600 from Leica. The sizes of the irregularly shaped constituent particles were expressed as the diameter of a circle with the same area as the particle. Table 4 lists the volume fraction, V_p, and the particle radius, r_p, of the constituent phases.

The size and density of the dispersoids in the two Mn-containing alloys AA 3103 and AA 8014 were analyzed in a scanning electron microscope (SEM) Zeiss Merlin equipped with an Oxford INCA EDS system. Samples for SEM were carefully polished by argon ion beam milling using a Hitachi IM4000 cross-section polisher and analyzed in back-scattered mode. The size and density of the second-phase particles were analyzed with the software package AZtecFeature from Oxford Instruments [29, 30]. Particles were automatically detected through their gray values in the back-scattered image, such that size and shape of the individual particles could be recorded automatically. The results are presented in table 4.

4. Model application

4.1. Modeling of yield stress and work hardening

Three case studies on AA 1110, AA 3103 and AA 8014 alloys were used to validate the model described in section 2. The measured solute concentration and particle data shown in tables 3 and 4 were used in these calculations. Table 5 shows the fixed material parameters that were used for all alloys. The model was calibrated to experimental flow curves of these alloys for temperatures ranging from 20 °C to 550 °C and at three different strain rates of 0.1, 1.0 and 10 s^{-1}.

A nonlinear optimization scheme was implemented to determine the fitting parameters of the model. In the present work, a 'random walk' optimization procedure is employed. Using the predefined ranges of the calibration parameters, a random value is chosen from the range for each of the parameters and the flow curve is calculated by solving the kinetic equation of state and the evolution equations together iteratively. A target function was formulated from the sum of the squared absolute deviations between the simulated and measured values. The value of this target function is minimized at every strain step over all the flow curves using the

Table 5. Fixed material parameters for all alloys in the current study.

Symbol	Description	Value	Units
b	Burgers vector	2.86×10^{-10}	m
μ	Shear modulus (at RT)	26.5	GPa
ν	Poisson's ratio	0.3	—
M	Taylor factor	3.06	—
D_0	Self-diffusion coefficient for aluminum	1.3×10^{-4}	$m^2\ s^{-1}$
ρ_x^0, $x = m, i, w$	Initial dislocation density	1.0×10^{11}	m^{-2}
d	Grain size	470 (AA 1110) 1000 (AA 3103) 1000 (AA 8014)	μm

Table 6. Calculated stress values at RT for each strengthening contribution to the yield stress for strain rates of 0.1, 1.0 and 10 s^{-1}. The predicted yield stress is computed according to equation (1).

Alloy	Strain rate (s^{-1})	Intrinsic stress, σ_{int} (MPa)	Forest dislocation stress, σ_{for} (MPa)	Solute stress, σ_{sol} (MPa)	Orowan stress, σ_{OR} (MPa)	Predicted yield stress, σ_{calc} (MPa)	Exp stress, σ_{exp} (MPa)
AA 1110	0.1	10	1.54	11.61	3.75	26.89	26.05
	1.0	10	1.54	13.58	3.75	28.87	25.24
	10	10	1.54	15.90	3.75	31.18	26.11
AA 3103	0.1	10	1.54	31.91	10.93	54.37	49.90
	1.0	10	1.54	35.35	10.93	57.82	56.60
	10	10	1.54	39.17	10.93	61.63	50.50
AA 8014	0.1	10	1.54	17.51	8.52	37.57	48.90
	1.0	10	1.54	20.01	8.52	40.07	36.40
	10	10	1.54	22.88	8.52	42.93	41.60

same set of calibration parameters. The simulation finally picks the set of parameters for which the sum of the differences between the experimental and simulated flow curves is at minimum. Since the parameters have strong nonlinear influences, it must be ensured that the global optimum is found within the physically admissible bounds for each parameter.

The calculated values of the RT yield stress are shown in table 6 along with the experimentally measured yield stress. The contribution of the difrerent strengthening mechanisms to the RT yield stress is also shown in table 6. The intrinsic stress at RT is assumed to be 10 MPa [23–25], while the particle stress at RT is equal to the Orowan stress in equation (14). The forest dislocation stress is assumed to be equal to the Taylor stress at yield, $\sigma_{for} = \alpha\mu b\sqrt{\rho_x^0 + \rho_m^0}$, $(x = i, w)$, using the values shown in table 5 and assuming $\alpha = 0.5$.

Among the three alloys analyzed, AA 1110 is by far the softest, with a RT yield stress below 30 MPa (table 6). The Orowan stress for AA 1110 is rather low, 3.75 MPa, which can be attributed to the relatively large particle size present in the alloy (table 4). The solute elements contribute between 11 and 16 MPa to the total yield stress.

AA 3103 has the smallest particle size (table 4) and therefore also has the highest Orowan stress of about 11 MPa (table 6). Compared to AA 1110, the contribution of solid

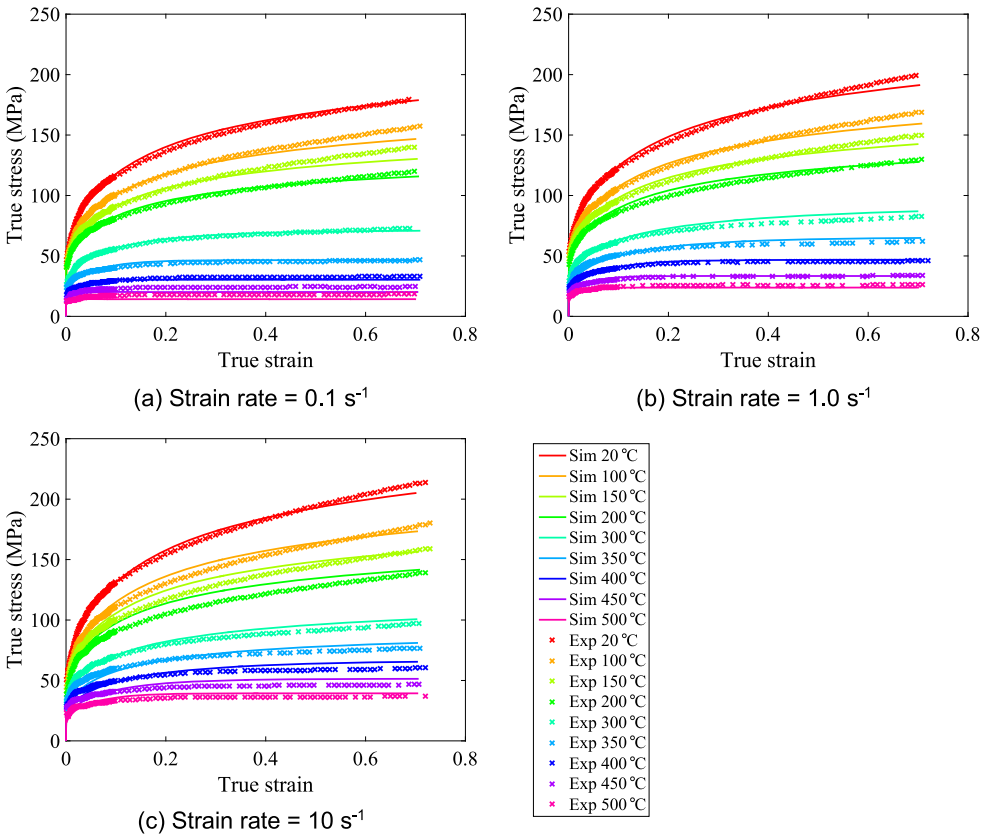

Figure 1. Comparison between experimental and computed flow curves for AA 3103 for temperatures in the range of 20 °C–500 °C and at three different strain rates (0.1, 1.0 and 10 s^{-1}).

solution strengthening to the yield stress is significantly higher, ranging from 32 to 39 MPa at RT. This is likely caused by the fairly large amount of Mn left in solid solution in AA 3103 (table 3). Thus, the total RT yield stress of AA 3103 is almost twice as high as that of AA 1110 (table 6). AA 8014 has a particle strength similar to that of AA 3103 at RT, but a much lower solute strength (table 6). Therefore, the total strength of AA 8014 lies in between the values of AA 1110 and AA 3103.

4.2. Modeling of yield stress and work hardening of AA 3103

In this section, the simulation of the yield stress and flow curves for the alloy AA 3103 are presented as a case study. The solute concentration and particle data of this alloy are given in tables 3 and 4 respectively; the model described in section 2 was used to fit the experimental flow curves of AA 3103 for temperatures ranging from 20 °C to 500 °C at three different strain rates of 0.1, 1.0 and 10 s^{-1}. The experimental and computed flow curves for AA 3103 are presented in figure 1. Using the optimization procedure described in section 4.1, a single parameter set was determined for the AA 3103 flow curves over all temperatures and strain rates. Overall, good agreement was achieved between the simulated and the experimental

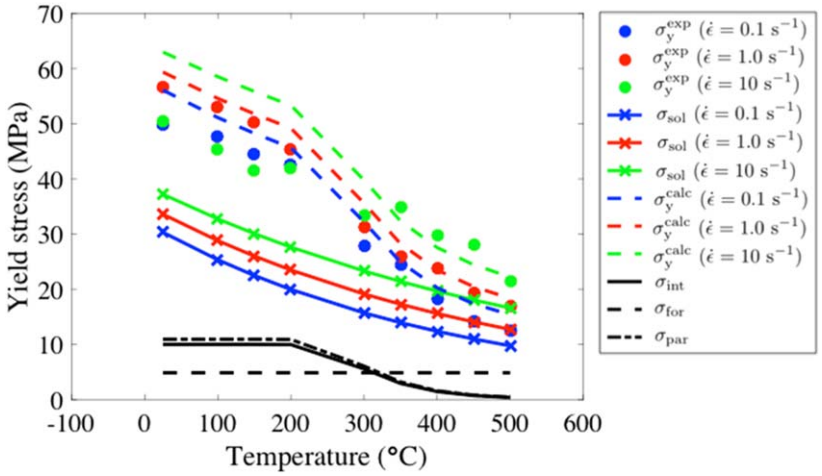

Figure 2. Comparison of measured yield stress (solid circles) and predicted yield stress (dashed lines) for AA 3103. Crosses correspond to the solid solution stress predicted using the solid solution strengthening model. The intrinsic, forest and particle stresses are also shown.

flow curves. At macroscopic strain values above 0.6, the simulated flow curves tended to be underpredicted compared to the measured flow curves. This is possibly due to barreling of the test specimen at high strains during the uniaxial compression tests.

The comparison between the measured and predicted yield stresses as a function of temperature is shown in figure 2. The solid circles denoted as $\boldsymbol{\sigma}_y^{\mathbf{exp}}$ correspond to the measured yield stresses from the experimental flow curves in figure 1, which were obtained using the standard 0.2% yield offset method. The crosses in figure 2 which are denoted as $\boldsymbol{\sigma}_{\mathrm{sol}}$, correspond to the calculated solid solution stress using equation (11). At RT, the solute elements contribute between 30 and 40 MPa to the overall yield stress of AA 3103, a value which decreases with increasing test temperature. Among the elements in solid solution, Mn has by far the largest effect, contributing about 90% of the total solid solution strengthening in AA 3103. For temperatures above RT, the temperature dependence of the intrinsic stress (equation (15)) and particle stress (equation (16)) was determined from the optimization procedure. The resulting curves for the intrinsic stress and particle stress as a function of temperature are also shown in figure 2. The predicted yield stress corresponds to σ_y^{calc} and was calculated using equation (1) using the solute, particle, forest and intrinsic stress contributions shown in figure 2. The comparison between the measured yield stress and the predicted yield stress for AA 3103 demonstrates that a reasonable fit was achieved between the simulated and the experimental values.

4.3. Comparison for AA1110, AA 3103 and AA8014

The procedure as described in sections 4.1 and 4.2 was repeated for AA 1110 and AA 8014. For each alloy, a separate calibration was performed using the model described in section 2 to evaluate the accuracy of the model for different chemical compositions and microchemistry states.

The quality of the individual calibrations for each alloy is summarized in table 7. All fits are comparable and within an excellent range, as quantified by the correlation coefficient, *C*,

Table 7. Accuracy of the model using an individual parameter set for each of the three alloys in the current study.

Alloy	Min flow stress, σ_{min} (MPa)	Max flow stress, σ_{max} (MPa)	Correlation coefficient, C	Mean squared deviation (MPa)	Mean abs. deviation $\Delta\sigma_{abs}$ (MPa)	Mean rel. deviation $\Delta\sigma_{rel}$ (%)
AA 1110	7.9	177.0	0.997	6.4	1.8	3.5
AA 3103	11.0	227.1	0.997	10.7	2.4	3.9
AA 8014	10.1	198.3	0.997	10.1	2.4	4.3

Table 8. Accuracy of the model applied to all the three alloys of the current study using a common set of parameters.

Alloys	Min flow stress, σ_{min} (MPa)	Max flow stress, σ_{max} (MPa)	Correlation coefficient, C	Mean squared deviation (MPa)	Mean abs. deviation $\Delta\sigma_{abs}$ (MPa)	Mean rel. deviation $\Delta\sigma_{rel}$ (%)
Combined	7.9	227.1	0.978	62.3	5.5	8.6

which exceeds 0.996. Since the solute content of each alloy is implicitly considered by the Leyson model, it is interesting to observe the effect of particles which is adjusted for each alloy during the calibration procedure. This could be a critical issue for the development of a unified model, which has to describe the influence of particle strengthening using a common set of parameters. In the present model, all types of particles are assumed to have the same effect on the flow stress.

4.4. Unified parameter set

The goal of this study is the development of a unified constitutive model, where the microchemistry of an alloy is an independent input. Thus, it should be possible to model different alloys within the composition range of the three sample alloys or consider variations in the chemistry or heat treatment of these alloys. Therefore, the flow curves for all three alloys were calibrated with a single set of parameters following the same procedure described in section 4.1. The predicted flow stresses for the complete set of measured data, consisting of 133 flow curves (17022 individual flow stress signals) are shown in figure 3. The computed flow stress for alloy AA 1110 is slightly overestimated, and for AA 3103 it tends to be slightly underestimated at higher values, but in total a good correlation is achieved. The overall accuracy of the calibration for all alloys is shown in table 8 and the values of the parameters are given in table A1 in the appendix.

As expected, the overall accuracy decreases slightly when the flow curves of all three alloys are calibrated with a single set of parameters instead of a specific set for each alloy. Since average fitting parameters are determined for all three alloys, there could still be alloy-specific influences that are not taken into account in the model. However, the overall quality of this model, with a correlation coefficient, C, of 0.978, can still be considered reasonable.

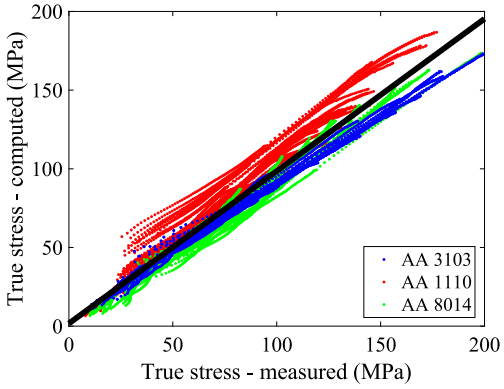

Figure 3. Correlation of experimental to computed flow stress for all alloys.

5. Model behavior and validation

A critical assessment of the results obtained in the three case studies shows that the current model is able to capture the yield stress and flow curves over a wide range of temperatures and strain rates with reasonable accuracy. The model gives meaningful predictions for the RT yield stress of all three alloys, including the well-known increase in yield stress with increasing strain rate (strain rate sensitivity, e.g. [31]). However, as shown in table 6, this trend is not so obvious in the experimental yield stress values. At increasing strain rates, it becomes more difficult to measure the yield stress during the elastic-plastic transition. Furthermore, minor deviations in the simulated flow curves observed at high strains may be attributed to barreling which is commonly observed in uniaxial compression tests.

With the conclusion that the current model behavior is able to capture the physics of work hardening for the alloys presented in section 4, an additional validation exercise was performed using pre-existing measurements on a set of six alloys. These six alloys was produced on a laboratory scale with controlled variations of the main alloying elements Mn (0.14–0.99 wt%) and Mg (0.34–4.39 wt%). The characterization of the microchemistry of these alloys is given in [32, 33]. In this study, the two variants with highest Mg content were excluded, since the validity of the model is questionable in this range; i.e. Portevin–Le Chatelier effects are not accounted for in the model. The composition of the remaining four laboratory alloys is summarized in table 9. All alloys were tested in uniaxial compression on the same equipment according to the same procedure described in section 3. As an example, figure 4 shows measured flow curves of the four alloys for an arbitrary temperature/strain rate combination.

With the previously determined set of parameters for the unified model on the three alloys of the current study (table A1 in the appendix), the measured flow curve fields of the laboratory alloys were computed, adjusting only the solute concentration and the particle contents of each alloy. Figure 5 shows the measured and computed flow stresses at forming conditions of 400 °C/1.0 s^{-1} at a constant strain of 0.5, which is well in the steady state region of each flow curve. Firstly, it is observed that the laboratory alloys are generally higher both in alloy and particle content, so that the model is actually extrapolated beyond the range

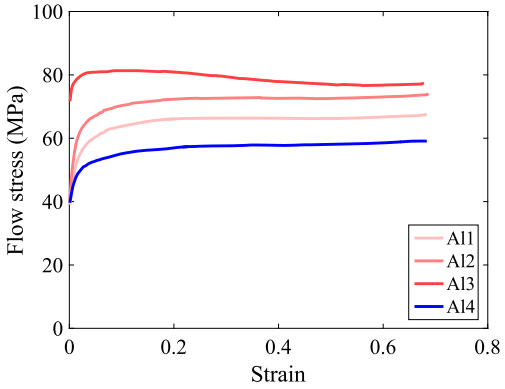

Figure 4. Measured flow curves for the laboratory alloys at a temperature of 400 °C and a strain rate of 1.0 s^{-1}.

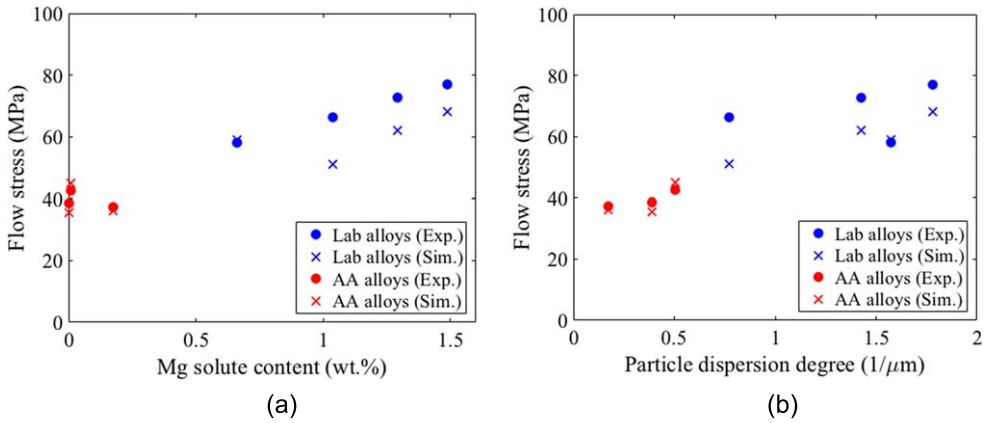

Figure 5. Comparison between experimentally measured flow stress and simulated flow stress for the laboratory alloys and AA alloys (AA 1110, AA 3103 and AA 8014) at 400 °C/1.0 s^{-1} at a macroscopic strain of 0.5.

Table 9. Composition of the laboratory alloys [32, 33].

	Measured alloy content (wt%)					Solid solution (at%)		Dispersoids	
Alloy	Si	Fe	Cu	Mn	Mg	Mg	Mn	r_p (nm)	V_p
Al1	0.17	0.33	0.003	0.16	0.97	1.1	0.02	80	0.008
Al2	0.17	0.33	0.004	0.45	0.98	1.1	0.08	65	0.018
Al3	0.19	0.35	0.008	0.98	1.02	1.1	0.1	65	0.028
Al4	0.19	0.32	0.004	0.45	0.46	0.5	0.09	50	0.013

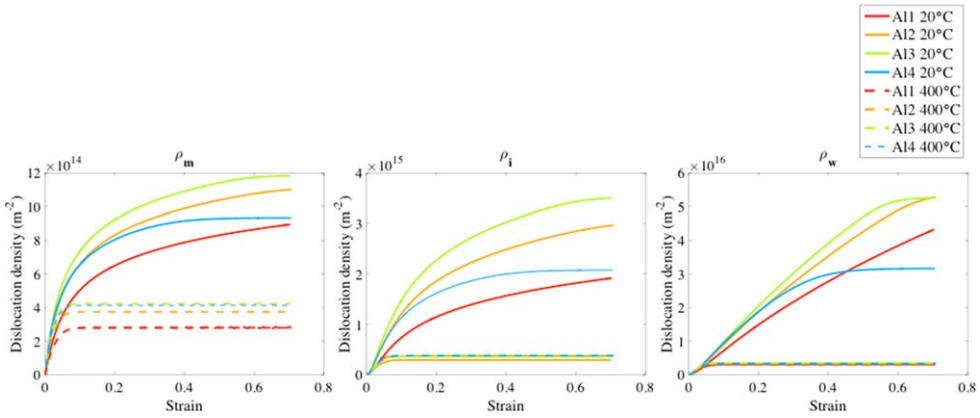

Figure 6. Computed dislocation densities for the laboratory alloys at two different temperatures, 20 °C and 400 °C, at a strain rate of 1.0 s^{-1}.

for which it was calibrated. Despite this fact, the model prediction is generally good. With increasing Mg content in solid solution, the flow stress increases. While for low Mg content the correlation is excellent, deviations are larger for Mg content further away from the valid range. The degree of particle dispersion takes into account the combined effect of particle volume content and particle size on strength and is defined as $\frac{\sqrt{3V_P/2\pi}}{r_P}$; see also equation (14). This parameter also exceeds the range of validity of the model, but the correct trend of flow stress with increasing particle dispersion degree is well described.

Using the current model, the evolution of the dislocation densities can also be computed if they cannot be measured experimentally. This is an important feature since the model is fast enough to run within a process model; e.g. of a rolling mill. Such an integrated rolling model then allows for an estimation of the rolling performance with a variation in alloy content or in previous heat treatments. In consecutive passes it also allows for a prediction of final properties as a consequence of a sequence of deformations where microchemistry variations may have highly nonlinear influences.

Using the solute concentrations for the laboratory alloys shown in table 9, the evolution of the dislocation densities for the laboratory alloys, at deformation temperatures of 20 °C and 400 °C are computed and shown in figure 6. The dislocation densities tend to increase with increasing solute content. All three dislocation densities reach a saturation state very early before 0.1 strain at 400 °C, whereas at 20 °C a continuous increase in the dislocation densities is observed. At 20 °C, the dislocation densities of the Al4 alloy also starts to saturate at a lower macroscopic strain of around 0.4. It is also noted that the immobile dislocation density in the cell wall, ρ_w, is much larger than both ρ_i and ρ_m, which is consistent with the observation that hard dislocation walls of high local dislocation density are separated by soft regions of low local dislocation density [34].

The absolute quality in predicting the laboratory alloys will most likely not allow for the usage of this current model within a process model, e.g. rolling, for these alloys. However, the model has the future potential of covering the range of common alloying elements and particle contents of non-heat treatable alloys within the relevant processing range of

temperatures, strains and strain rates. A future calibration over a wider range of alloys will certainly improve the quality of the flow stress predictions considerably.

While the classical Taylor's relation (equation (27)) was adopted for work hardening in the current model, different forms of this equation can be derived from atomistic and discrete dislocation dynamics approaches to resolve details of the underlying dislocation dynamics and the dislocation interactions between different slip systems [35–37]. The implementation of these equations for the flow stress in our current model will be an interesting direction for future work.

Nevertheless, the present model represents a major step towards a microchemistry-dependent unified model of flow stress which is required for a complete through-process modeling framework. Generation of alloy-dependent microchemistry information using a suitable microchemistry model, such as in [38, 39], will allow for a prediction of flow stress for situations where experimental flow curves are not available. Minor fluctuations in an industrial process, e.g. temperature fluctuations in furnaces or slight variations in alloy content, can be accounted for in this model.

6. Conclusions

A fast statistical microchemistry-dependent model was developed to simulate the yield stress and flow curves of commercial Al alloys over a wide range of temperatures and strain rates. The model was applied to three different non-heat treatable wrought Al alloys: AA 1110, AA 3103 and AA 8014. These three case studies demonstrate how microchemistry information such as the solute concentration, particle volume fraction and particle size can be incorporated into a statistical internal state variable model for an accurate simulation of the flow stress of different non-heat treatable Al alloys.

The present microchemistry-dependent model is able to reproduce the experimental flow curves with reasonable accuracy across a wide range of temperatures and strain rates while using a single set of constants for solute strengthening. The best quantitative descriptions of the experimental flow curves were achieved when the alloys were calibrated individually, but a reasonable accuracy was also achieved with a unified model, where all three alloys were calibrated with a single set of parameters.

In conclusion, the present microchemistry-dependent model represents a major step towards alloy-dependent prediction of materials properties and mechanical response that is advantageous in alloy design as well as process and property optimization, e.g. within a through-process modeling framework for Al rolling [40].

Acknowledgments

Helpful discussions with Dr G P M Leyson are gratefully acknowledged.

Appendix

Table A1. Model parameters calibrated individually for AA 3103, AA 1110 and AA8014; and for all the alloys combined. The equations corresponding to these parameters can be found in [5].

Description	Symbol	Values for AA 3103	Values for AA 1110	Values for AA 8014	Values for all alloys	Units
Number of active slip systems	n	5.573	7.984	7.985	4.797	—
Passing coefficient for shear	α	0.192	0.224	0.437	0.152	—
Volume fraction of cell walls	f_w	0.810	0.901	0.790	0.945	—
Average number of dislocation spacings a dislocation travels in cell interior	β_i	12.909	40.666	22.927	9.152	—
Average number of dislocation spacings a dislocation travels in cell wall	β_w	85.575	56.080	56.488	6.634	—
Critical distance for annihilation	d_{anni}	3.104	1.970	5.602	5.632	b
Critical distance for climb	d_{climb}	4.659	8.388	10.007	8.896	b
Critical distance for lock formation	d_{lock}	4.762	4.001	10.006	10.008	b
Critical distance for immobilization	d_{imm}	0.054	0.189	0.0988	0.199	b
Activation energy for slip	Q_{slip}	2.554	2.528	2.078	2.763	eV
Activation energy for climb	Q_{climb}	1.341	1.259	1.1761	1.354	eV
Activation energy for cross slip	Q_{cross}	1.429	1.420	1.499	1.499	eV
Scaling factor for cross slip	a_{cross}	21.349	14.477	31.176	15.827	—
Scaling factor for clearing effect	a_{clear}	0.897	0.4766	0.9890	0.9993	—
Critical temperature	T_{crit}	572.68	614.41	610.836	593.911	K
Exponent for transition from looping to climb	A	7.299	6.592	4.314	4.506	—

b = Burgers vector (2.86×10^{-10} m).

ORCID iDs

Su Leen Wong https://orcid.org/0000-0002-2178-492X
Thiemo Brüggemann https://orcid.org/0000-0001-6477-2673

References

[1] Roters F, Raabe D and Gottstein G 2000 Work hardening in heterogeneous alloys—a microstructural approach based on three internal state variables *Acta Mater.* **48** 4181–9
[2] Karhausen K F and Roters F 2002 Development and application of constitutive equations for the multiple-stand hot rolling of Al-alloys *J. Mater. Process. Technol.* **123** 155–66
[3] Goerdeler M, Crumbach M, Schneider M, Gottstein G, Neumann L, Aretz H and Kopp R 2004 Dislocation density based modelling of work hardening in the context of integrative modelling of aluminium processing *Mat. Sci. Eng.* A **387–389** 266–71
[4] Mohles V, Li X, Heering C, Hirt G, Bhaumik S and Gottstein G 2008 Validation of an improved dislocation density based flow stress model for Al-alloys *Int. J. Mater. Form.* 77–80
[5] Prasad G 2007 An improved dislocation density based work hardening model for Al-alloys *PhD Thesis* RWTH Aachen University (Germany)
[6] Kocks U F, Argon A S and Ashby M F 1975 Thermodynamics and kinetics of slip *Prog. Mater Sci.* **19** 1–281
[7] Ashby M F and Jones D R H 1980 *Engineering Materials—an Introduction to Their Properties and Applications* (Oxford: Pergamon) pp 97–102
[8] Myhr O R, Grong Ø and Anderson S J 2001 Modelling of the age hardening behaviour of Al–Mg–Si alloys *Acta Mater.* **49** 65–75
[9] Leyson G P M, Curtin W A, Hector L G Jr and Woodward C F 2010 Quantitative prediction of solute strengthening in aluminium alloys *Nat. Mater.* **9** 750–5
[10] Leyson G P M, Hector L G Jr and Curtin W A 2012 Solute strengthening from first principles and application to aluminum alloys *Acta Mater.* **60** 3873–84
[11] Leyson G P M and Curtin W A 2016 Thermally-activated flow in nominally binary Al–Mg alloys *Scr. Mater.* **111** 85–8
[12] Leyson G P M and Curtin W A 2016 Solute strengthening at high temperatures *Modelling Simul. Mater. Sci. Eng.* **24** 065995
[13] Fleischer R L 1966 Substitutional solution hardening of copper *Acta Metall.* **14** 1867–8
[14] Labusch R 1970 A statistical theory of solid solution hardening *Phys. Status Sol.* **41** 659–69
[15] Diak B J, Upadhyaya K R and Saimoto S 1998 Characterization of thermodynamic response by materials testing *Prog. Mater Sci.* **43** 223–363
[16] Caillard D and Martin J L 2003 *Thermally Activated Mechanisms in Crystal Plasticity* (Oxford: Pergamon)
[17] Argon A S 2007 *Strengthening Mechanisms in Crystal Plasticity* (Oxford: Oxford University Press)
[18] Deschamps Y B 1999 Influence of predeformation and ageing of an Al–Zn–Mg alloy: II. Modeling of precipitation kinetics and yield stress *Acta Mater.* **47** 293–305
[19] Friedel J 1964 *Dislocations* (Oxford: Pergamon)
[20] Martin J W 1980 *Micromechanisms in Particle-Hardened Alloys* (*Cambridge Solid State Science Series*) (Cambridge: Cambridge University Press)
[21] Voyiadjis G Z and Almasri A H 2008 A physically based constitutive model for fcc metals with applications to dynamic hardness *Mech. Mater.* **40** 549–63
[22] Carreker R P Jr and Hibbard W R Jr 1953 Tensile deformation of high-purity copper as a function of temperature, strain rate and grain size *Acta Metall.* **1** 654–55 657–63
[23] Kamikawa N, Huang X, Tsuji N and Hansen N 2009 Strengthening mechanisms in nanostructured high-purity aluminium deformed to high strain and annealed *Acta Mater.* **57** 4198–208
[24] Cahn R W and Haasen P 1996 *Physical Metallurgy* 4th edn (Amsterdam: North-Holland Physics)
[25] Huskins E L, Cao B and Ramesh K T 2010 Strengthening mechanisms in an Al–Mg alloy *Mater. Sci. Eng.* A **527** 1292–8
[26] Dong Y and Curtin W A 2012 Thermally activated plastic flow in the presence of multiple obstacle types *Model. Simul. Mater. Sci. Eng.* **20** 075006

[27] Engler O, Clark M, Löchte L and Lok Z 2008 Multi-temperature measurement of thermoelectric power for characterisation of solute levels in multi-component industrial aluminium alloys *Aluminium* **84** 92–5
[28] Engler O, Laptyeva G and Wang N 2013 Impact of homogenization on microchemistry and recrystallization of the Al–Fe–Mn alloy AA 8006 *Mater. Char.* **79** 60–75
[29] Lang C, Hiscock M, Holland J, Yamaguchi S, Joyce D and Vatougia G 2015 New developments in automated particle analysis in the electron microscope—from micro to nano *Microsc. Microanal.* **21** 337–8
[30] Engler O, Kuhnke K and Westphal K 2019 Development of second-phase particles during solidification and homogenization of aluminium alloy AlMn1 *Pract. Metallogr.* **56** 317–41
[31] Lademo O-G, Engler O, Aegerter J, Berstad T, Benallal A and Hopperstad O S 2010 Strain-rate sensitivity of aluminium alloys AA1200 and AA3103 *J. Eng. Mater. Technol.* **132** 041007-1–8
[32] Mülders B 2001 Modellierung der Verfestigung technischer Aluminiumlegierungen *PhD Thesis* RWTH Aachen University(Germany)
[33] Crumbach M 2005 Through-process texture modelling *PhD Thesis* RWTH Aachen University (Germany)
[34] Mughrabi H 1983 Dislocation wall and cell structures and long-range internal stresses in deformed metal crystals *Acta Metall.* **31** 1367–79
[35] Devincre B, Hoc T and Kubin L 2008 Dislocation mean free paths and strain hardening of crystals *Science* **320** 1745–8
[36] Devincre B, Kubin L and Hoc T 2006 Physical analyses of crystal plasticity by DD simulations *Scr. Mater.* **54** 741–6
[37] Zhu Y, Xiang Y and Schulz K 2016 The role of dislocation pile-up in flow stress determination and strain hardening *Scr. Mater.* **116** 53–6
[38] Liu Z, Mohles V, Engler O and Gottstein G 2014 Thermodynamics based modelling of the precipitation kinetics in commercial aluminium alloys *Comput. Mater. Sci.* **81** 410–7
[39] Lentz M, Laptyeva G and Engler O 2016 Characterization of second-phase particles in two aluminium foil alloys *J. Alloys Compd.* **660** 276–88
[40] Hirsch J, Karhausen K F and Engler O 2004 Property control in production of aluminum sheet by use of simulation *Continuum Scale Simulation of Engineering Materials* ed D Raabe *et al* (New York: Wiley) pp 705–25